batteries

MDPI

Article

Design Analysis of 26650 and 18650 LFP Cells for High Power and Low Temperature Use Cases

Florian Wätzold [1,2,*], Anton Schlösser [1], Max Leistikow [3] and Julia Kowal [1,*]

[1] Electrical Energy Storage Technology, Technische Universität Berlin, Einsteinufer 11, 10587 Berlin, Germany
[2] Stefan Wätzold Projekt GmbH, Mottlaupfad 15, 13503 Berlin, Germany
[3] Faculty V Mechanical Engineering and Transport Systems, Universität Berlin, Straße des 17. Juni 135, 10623 Berlin, Germany
* Correspondence: waetzold@campus.tu-berlin.de (F.W.); julia.kowal@tu-berlin.de (J.K.)

Abstract: This study investigates the design and geometric properties of high-power and low-temperature 18650 and 26650 lithium iron phosphate (LFP) cells. The analysis focuses on the geometry and components' thicknesses and deriving CAD models for both cell formats. Design variations were observed, even within cells from the same manufacturer. For instance, one manufacturer's 26650 cell was not a scaled-up version of their 18650 cell, and no equivalence was found between the designs of high-power and low-temperature cells from the same manufacturer. Thus, modifications are not purely chemistry based. The results also reveal deviations from the literature values for jelly roll component thicknesses, with anode current collectors averaging 61 µm and cathode current collectors averaging 60 µm. Coating thicknesses varied, with anode coatings averaging 32 µm and cathode coatings averaging 52 µm. These variations in current collector and coating thicknesses suggest that both high-power and low-temperature LFP cell designs differ from the typical literature values. Furthermore, a trade-off was observed between low-temperature operation with two-tab designs and high pulse capability with limited minimum operating temperatures. Additionally, smaller particle sizes in anode coatings were associated with lower impedance.

Keywords: high-power LFP cell; low-temperature LFP cell; geometrical analysis; 18650 CAD model; 26650 CAD model

Academic Editors: Kamil Burak Dermenci and Pascal Venet

Received: 10 December 2024
Revised: 8 January 2025
Accepted: 16 January 2025
Published: 20 January 2025

Citation: Wätzold, F.; Schlösser, A.; Leistikow, M.; Kowal, J. Design Analysis of 26650 and 18650 LFP Cells for High Power and Low Temperature Use Cases. *Batteries* **2025**, *11*, 38. https://doi.org/10.3390/batteries11010038

1. Introduction

In the evolving world of cylindrical cell formats, understanding the delicate balance between geometry and chemistry is key to identifying superior cell formats. Different cylindrical cell formats are usually named by diameter (mm), length (mm), and cylindrical symbols. One of the common cell formats is 18650 [1], and increasing cell size is associated with higher energy density because of better volume utilisation [2]. New cell concepts are up to 46 mm in diameter and 80 mm [3] or even 120 mm [4] in length. While the outside geometries are defined by standards [5], the inside geometries are defined by the manufacturer and chosen chemistry. Regarding the latter, this study focuses on cells with cathodes using lithium iron phosphate (LFP), which was patented in 1996 and is used for its chemical and thermal resistance [6] as well as its low relative price [7]. Usually for these LFP cells, graphite for the anode and lithium hexafluorophosphate dissolved in carbonate as electrolyte is used [8]. The current collectors are usually made of nickel or copper for the anode and aluminium for the cathode as described in the chapter Design of Battery Cells. To improve the suitability for power applications, either the active materials can be doped for enhancing the diffusion coefficient or the electrode materials can be nanostructured

to reduce the diffusion length [9]. For low-temperature operations, it is reported that nanostructures within the graphite can reduce the dendrite formation, reduced LFP particle sizes can obtain the capacity, solid polymer electrolytes offer higher thermal stability, and separators with lithium-rich material ensure ion conductivity [10].

Due to the relative high power density compared to lead-acid, LFP is suitable for applications such as starter lightning ignition batteries [11]. Starter batteries must fulfil various requirements, which are defined, for instance, in DIN EN 50,342. For LFP, four cells in a serial configuration are necessary to encompass the voltage range of 14.2 to 7.2 V. Furthermore, resistance to deformation [1] and cold-cranking pulses of at least 9C [12] warrant particular attention. The functionality must be maintained across the operating temperature range of an automobile, which extends from −30 [13] to +85 °C [14]. When optimising the volume and mass of these batteries, utilising the package determines the cell requirements.

There is also a trade-off between energy and power cells, and with respect to the inner geometry it is apparent that theoretically thin electrodes with high porosity, large total surface area, and small particle size offer higher currents due to shorter diffusion paths [15]. Thicker current collectors have higher electrical conductivity and better heat transfer capabilities, resulting in higher power density and mechanical integrity [16]. High-power cell analysis showed that current collector and separator thicknesses are based on the thinnest available materials rather than being optimised for power or energy [17]. As no comprehensive analysis of high-power and low-temperature LFP cell geometries is known to the authors, and published geometrical properties vary over a wide range, as summarised in the next chapter, five state-of-the-art cells were examined. Four of these are suggested for high-power and one for low-temperature applications and are compared to the range of published findings.

Design of Battery Cells

Figure 1 shows a simplified assembly of a battery cell cut section. Negative (1) and positive (2) terminals provide the electrical connection. Wound layers of two electrodes interleaved with two separators (3), known as jelly roll, are soaked in an electrolyte to facilitate energy storage. Electrodes can be categorised as anodes (negative) and cathodes (positive) [6]. The cathode features of a current collector (4) are coated on both sides with LFP (5) and one positive tab (6). The anode, recommended to be designed longer than the cathode [18], mirrors this design with its current collector (7), coating (8), and negative tab (9). A centre pin (10) supports the assembly and venting [19] and minimises the deformation of the hollow in the jelly roll [20]. For the electrical connection, the positive tab is linked to the cell top via the current interrupting device (11), which disconnects the cell in critical conditions, and the safety vent (12), which alleviates overpressure. To seal the cell and isolate the positive from the negative terminal, a gasket (13) is deployed. An insulator (14) only displayed at the cell bottom mitigates short circuits by separating the conductive electrodes, and the enveloping can (15) provides structural support and connects the negative tab and terminal.

Three aspects of the cells must be detailed to evaluate the cells. The cell core is the jelly roll storing energy, tabs conducting current, and the cell top ensuring electrical connection and safety. Published properties especially thicknesses and material per component are presented in Table 1.

Table 1. Findings regarding thickness and material of centre pin, anode, separator, tabs, cathode and can (not mentioned aspects marked with /).

Source	Cell	Centre Pin	Anode Coating	Anode Current Collector	Separator	Cathode Coating	Cathode Current Collector	Tabs	Cell Top	Can
[20]	18650 (Li-Ion)	Geometry: 50 mm length, diameter 3 mm, thickness 0.1 mm	Geometry: Diameter of the jelly roll hollow 3.5 mm and diameter of the jelly roll 18 mm Material: Elastic Modulus (GPa): 1.1, Poisson's ratio: 0.5, Density (kg/m^3): 0.9, Yield Strength (MPa): 31.0, Tensile Strength (MPa):/					Ni-tab: Thickness 0.1 mm, width 4 mm Material: Ni—according to ABAQUS' user manual, Elastic Modulus (GPa): 2.19, Poisson's ratio: 0.31, Density (kg/m^3): 8900, Yield Strength (MPa): 148, Tensile Strength (MPa): 462 Al-tab: Thickness 0.1 mm, width 3 mm Material: Al—according to ABAQUS' user manual, Elastic Modulus (GPa): 1.78, Poisson's ratio: 0.35, Density (kg/m^3): 2700, Yield Strength (MPa):/, Tensile Strength (MPa): 551	/	Geometry: Thickness 0.25 mm Material: Elastic Modulus (GPa): 166.7, Poisson's ratio: 0.3, Density (kg/m^3): 7860.0, Yield Strength (MPa): 291.9, Tensile Strength (MPa): 354.7
[21]	LG MJ1 18650	/	/	/	/	/	/	/	Geometry: Thickness insert current collector 0.497 mm and depth of its notch groove 0.413 mm. Minimum thickness at notch groove bottom 0.084 mm. Thickness burst disc 0.314 mm and groove depth 0.258 mm. Minimum thickness at groove bottom burst disk 0.056 mm. Cap thickness burst disk 0.303 mm and groove depth 0.237 mm. Minimum thickness at groove bottom 0.066 mm.	/
[22]	18650 (Samsung SDI INR18650 35E—high energy)	/	Geometry: Changed thickness from 174 µm to 252 µm reported via postmortem analysis.		/	Geometry: Unchanged thickness of 157 µm reported via postmortem analysis.		/	/	/
[23]	/	/	Geometry: Thickness-coated foils 0.1–0.2 mm. Metal foils contribute 10–15 µm each, remaining thickness of graphite or lithium metal oxide or phosphate powder. Thickness polymeric 10–25 µm. Material: Coated copper, and aluminium foils kept apart by polymeric separator. Coating is a mixture of active powders and binder soaked in electrolyte.					/	/	/
[24]	18650 high-power	/	Geometry: Anode thickness 47.7 µm		/	/	/	/	/	/
[2]	18650 and 21700	/		Geometry: 10 µm	/	/	Geometry: 20 µm	/	/	/
[25]	21,700 and 18650	/	Geometry: 21,700 high power and 18650 high power anode thicknesses of 65 µm and 34 µm, respectively.		/	/		/	/	/
[19]	/	/	/	/	/	/	/	Geometry: Positive tab thickness 0.08–0.15 mm Material: Aluminium Geometry: Negative tab thickness 0.04–0.1 mm Material: Nickel	/	/

Table 1. *Cont.*

Source	Cell	Centre Pin	Anode Coating	Anode Current Collector	Separator	Cathode Coating	Cathode Current Collector	Tabs	Cell Top	Can
[26]	Sanyo 18650	/	/	/	/	/	/	Geometry: Thickness Al-tab 0.104–0.097 mm	/	/
[3]	18650, 21,700, 2070 and 4680 cells	/	Geometry: Anode thickness 325.23 µm and cathode thickness 326.37 µm. Standard deviations more significant than electrode coating tolerances varying between ±2 µm and ±5 µm. Randomly selected positions resulted in thicknesses of separator 11 µm, cathode coating 52.5 µm, anode coating 82.5 µm, aluminium current collector 25 µm, and copper current collector 10 µm, resulting in a composite thickness of 327 µm.					/	/	/
[27]	/	/	/	/	Geometry: Thinner 25 µm and there are examples of 12 µm thin (with low mech. strength)	/	/	/	/	/
Range thicknesses		See [20]	82.5–185 µm, but 38 µm (assuming 48 µm −10 µm for high power) and potential 45% increase after use	10–15 µm	10–25 µm	52.5–185 µm	10–25 µm	40–150 µm	See [21]	See [20]

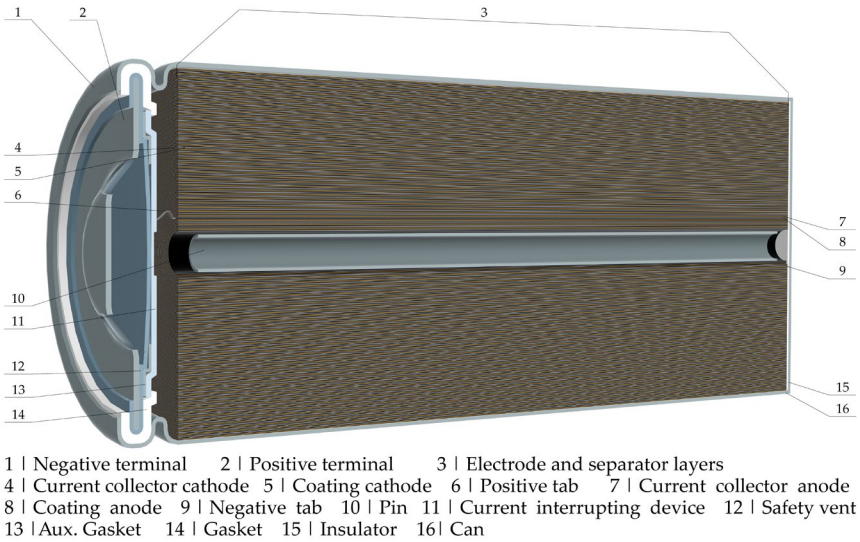

Figure 1. Schematic cross-section of simplified cylindrical cell.

Regarding the thicknesses of the jelly roll elements, those papers indicate a thickness of approximately 33 µm assuming a current collector thickness of 15 µm, to 82.5–185 µm for the anode coating and 52.5–185 µm for the cathode coating. Typical coating thicknesses vary from 50 to 300 µm [19], with an average variation of approximately 4 µm [26]. For high-power cells, more porous materials are used, whereas for energy cells, the anodes do not exhibit similar coherence [17]. In addition to the lower mechanical integrity issues owing to volume changes, the power density also decreases with electrode thickness [28]. Experiments with pouch cells show that with decreasing electrode thickness, the high-current-discharge performance increases, whereas the pulse-discharge power density for a low state of charge increases [29]. Recent studies have emphasised the importance of the anode for low-temperature operations [30–32]. For higher performance, thin separators are also recommended, and a review found that separators reduce the wall thickness to 12–20 µm with the disadvantage of lost mechanical strength [27].

Conductive stripes extend from the electrodes to connect to the terminals. Typically, these tabs are welded to the electrodes before winding [19]. A numerical model of wound potential-pair continua concluded that fewer tabs in current collectors result in longer current pathways, thereby increasing cell impedance [33]. A tear-down of 19 cylindrical cells revealed that one or two tabs per electrode are typically used [3]. It was also found, that a negative tab at the end or two negative tabs in parallel and the positive tab located in the middle showed the lowest impedance increase, slightest cracks of cathode materials, and best structural integrity of the graphite anode compared to a positive tab opposite to the negative tab or a positive tab in the middle of the electrodes [34]. It was also found that using multiple tabs per current collector can reduce internal inhomogeneities such as current density or mechanical stress [35]. New designs such as Tesla's 46,800 mitigate the ohmic losses of jelly roll [36] by engineering it in a tabless manner, with a quarter of the electrodes not connected to the tab [3].

Reviewing cap designs, it was found that different designs were used for activation mechanisms [21]. From an engineering perspective regarding the LG cell patent [37], the main feature of the cell top is the current-interrupting device that connects the tabs to the cell top. It is in contact with the safety vent. Current interrupt devices and safety vents exhibit material weakening, which interrupts the contact in the case of increasing pressure in the range of 0.998–2.285 MPa at 100 °C [21]. Both are insulated by an auxiliary gasket and gasket from the can. The top is closed by the top cap which is also insulated by the gasket and is in contact with the safety vent, which enables electrical flow.

2. Materials and Methods

2.1. Methodology

The design analysis consists of six steps. First, the cells must be selected, and secondly an approach to measure the design specifics must be decided. Third, an initial charging test is required to confirm that the cells are fully functional. Fourth, the CT scanner needs to be set up, and the cells scanned to identify any inhomogeneities. Finally, the cells can be subjected to tear-down after the scan and further electrical/thermal tests. In the sixth step, measurements from the scans and tear-down can be evaluated.

In addition to geometrical insights, hypotheses for examination can be validated.

- Usually, high power cells are not examined regarding thicknesses.
- 26650 are extended 18650 cells.
- Low-temperature cells are based on existing formats with adjusted chemistry.

2.2. Selection of LFP Cells

An overview of the selected cells is presented in Table 2 based on the data sheets and the measured weight, length, and diameter of the cells. The main criterion was the ability to provide high discharge pulses, which led to the selection of the following cells. For identification purposes they are referenced by a colour code: red (IFR26650-25B), green (ANR26650M1B), orange (APR18650M1B), or blue (IFR26650P2.5Ah). One more cell, grey (IFR26650LT3.0Ah), was added because of the advertised low-temperature properties to validate whether these properties are achieved only by chemical changes or require an adjusted design. The benefit of selecting green and orange from one supplier is that different cell sizes may use the same components and especially the same thicknesses for the jelly roll layers.

Table 2. Key specification of selected LFP cells (measured marked with * and from data sheet marked with ~).

Cell ~	Code	Length in mm *	Diameter in mm *	Weight in g *	Capacity in Ah ~	Voltage in V ~	Impedance in mOhm	Max Pulse Discharge Current in A ~	Temperature Range in °C ~
IFR26650-25B	red	66.04	26.08	82.8	2.5	2–3.65	6	75	−20 to +70
ANR26650M1B	green	65.41	25.95	75.2	2.56	3.3	6	120	−20 to +60
APR18650M1B	orange	64.97	18.37	41.6	1.2	3.3	12.6	50	−40 to + 60
IFR26650P2.5Ah	blue	65.87	26.16	84.5	2.5	3.2	7	75	−20 to +60
IFR26650LT3.0Ah	grey	66.39	26.37	85.4	3	3.2	9	30 (≥−20 °C)/ 21 (<−20 °C)	−50 to 60

2.3. Selection of Analysis Approach

The purpose of the measurements was to determine the geometries of the cell case, cell top, and jelly roll geometries. Therefore, the measurements were performed in stages. First, a CT scan of the pristine cell and subsequent cell tear-down of the cell after the electrical tests were performed.

A typical dimensional measurement task for CT applications is thickness analysis of the cell assembly [38]. CT scans have also been used to evaluate the degradation of electrodes over charge–discharge cycles [39] and to track the delamination and deformation of jelly rolls [26]. To measure the electrode thickness, a sub-micrometre scan with a resolution of 5–10 µm is recommended [40]. However, it should be noted that the measurement results are only an approximation of the measurand value [41] as, for example, different cell materials attenuate X-ray beams differently and also the distance to the detector varies in each step. Wall thickness analyses based on CT are particularly sensitive to threshold values because the resultant measurement errors affect both sides of the measured wall and

are usually insensitive to scale errors if the measured wall is thin compared to the overall object dimensions [38].

Additionally, a tear-down analogue to [42,43] was performed to provide insights into other properties, such as the material composition and additional measurements of the electrodes with higher precision as the CT scans. For the latter, a micrometre screw and laser scanning microscope of the cutout parts were used.

2.4. Initial Electrical Testing

As cycled cells exhibited a gradually increasing bending of the jelly roll towards the cell centre [26,39], new cells were used for the examination. To indicate full functionality and a comparable extension of the cell components, all cells were initially fully loaded, as experiments have found that the thickness of the anode swells by approximately 8.5% during charging and the thickness of the cathode swells by approximately 3.5% during discharging [20]. The voltage profile during the initial charging process of each cell, according to the data sheet, is shown in Figure A1 in Appendix A. No abnormalities were found, indicating a defect in the cells. After successful charging, the cell capacity was determined and compared to the nominal capacity. Red and orange exceeded their nominal capacity with 102.98 and 101.73%, while grey, blue, and green reached 98.98, 96.65, and 94.58%, respectively. After confirming that the cells were fully operational, they were discharged for the CT scan.

2.5. Setup and CT Scans

For efficiency reasons and as differentiation, aside from the tabs at the bottom and the insulator visible during tear-down, can primarily be assessed in the upper part of the battery cell, this section focuses on the CT scans. The main aim was to evaluate the design of the cell cap and derive insights on the jelly roll and its peculiarities. To achieve this, the red, orange, blue, and grey cells were scanned with a cone beam scan of the upper cell part and the green cell was scanned with a helical scan, completing the representation of the total cell. Balancing the energy requirements for penetration of the steel, aluminium and copper sheets with the consequent scan artefacts posed a challenge across all five cells.

At room temperature, the five battery cells were subjected to a micro-tomographic analysis at the Natural History Museum Berlin (Laboratory identification ID SCR_022585) using a Comet YXLON FF85 (Comet YXLON GmbH, Hamburg, Germany; Equipment identification ID SCR_020917) at 250 kV and 140 µA for the cone beam scan and 160 µA for the helical scan, generating 2500 projections for the cone beam scan and 5588 projects for the helix scan with 1 s per scan. These parameters were selected based on previous scans utilising the FF85 scanning objects of comparable size or material composition and subsequently adjusted for the orange, green, and grey cell in three test scans each to ensure complete X-ray penetration with minimised artefacts and sufficient contrast.

The different voltages and projection settings, depending on the respective specimen size, resulted in the effective voxel size of approximately 10.588 µm, representing the minimum defined by cell diameter and the conical shape of the beam in the FF85. The reconstruction of the voxels was performed using the Nexus reconstruction software (Comet YXLON GmbH, Hamburg, Germany), and the data were visualised using VG Studio Max 3.5 (Volume Graphics GmbH). The results of the scans showing the upper cell part are shown in Figure 2. Four of the five cells exhibited a characteristic bend at the transition from the can to the top of the cell and displayed a domed terminal structure.

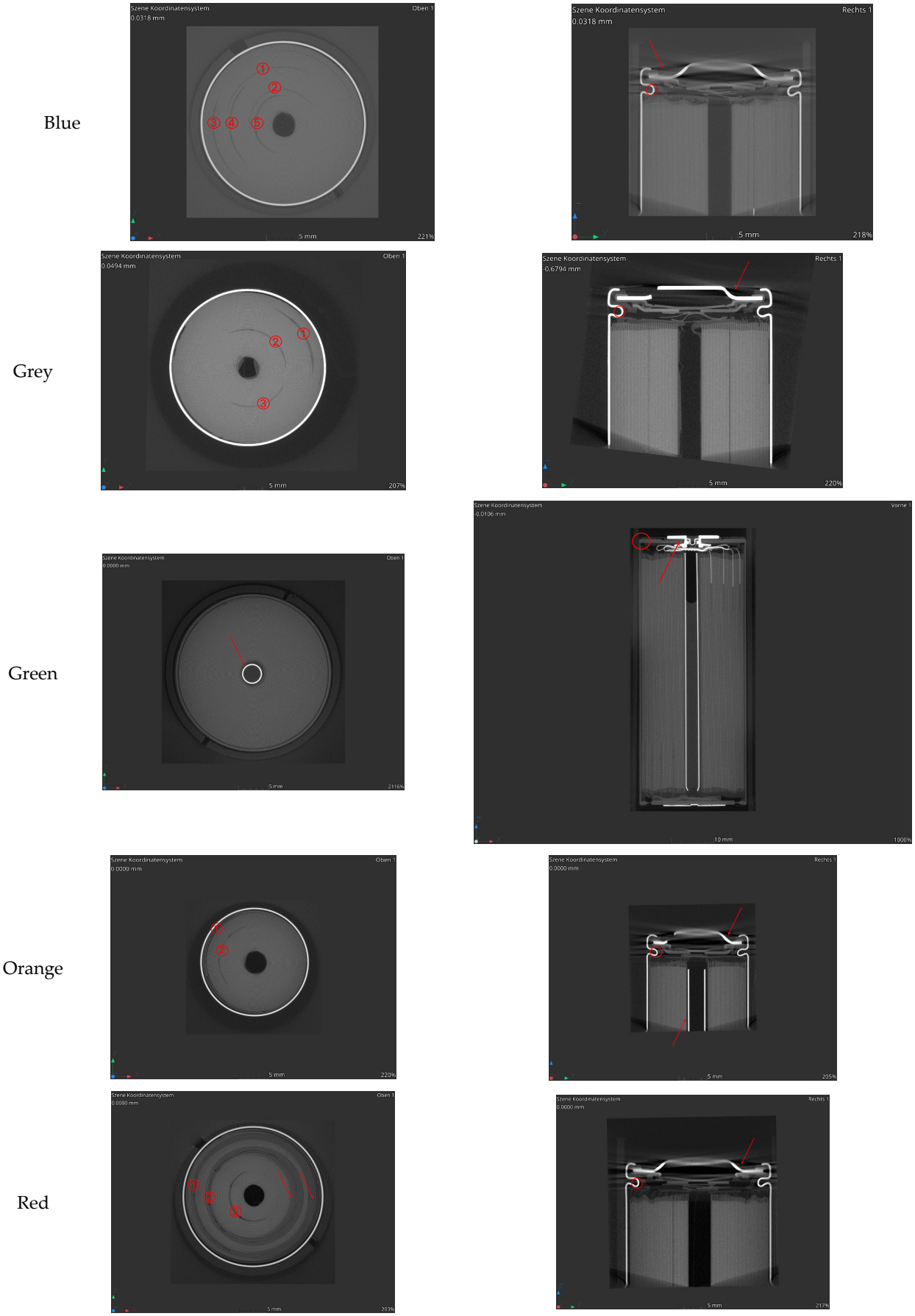

Figure 2. CT results of cell top.

The number of jelly roll windings ranged from 36 (grey), 39 (green), and 42 (blue) to 43 (red) for the 26650 s and was 26 (orange) for the 18650. The blue cell shows five inhomogeneities due to the tabs, with a distinct bend at the can-top transition and a domed terminal. Additionally, there are two extra inhomogeneities, likely related to the tabs on the opposite side. The grey cell has three inhomogeneities linked to tabs, a similar characteristic bend at the can-top transition, and a less pronounced terminal dome compared to the blue cells. The green cells stand out as they show no visible inhomogeneities, feature a central pin, lack the characteristic bend at the can-top transition, and have a straight T-shaped terminal instead of the typical dome. In addition, the colour of the can is darker than the grey scale values of the other cell cans. In addition to the top structure, the helical CT scan of the total cell provides detailed insights into the lower section of the cell, including the tapered pin that terminates at the level of the cathode layer. This allows a clear visualisation of the tabs linked to the bottom of the cell and the corresponding external terminal. The orange cell displays a central pin, an inhomogeneity caused by tabs, shadows on the outermost windings, a characteristic bend at the can-top transition, and a domed terminal. Finally, the red cells exhibit three inhomogeneities due to tabs, with additional shadows observed at the mid-winding and edge. These cells also exhibit a characteristic bend at the can-top transition and a domed terminal.

For CT analysis, VG Studio Max 3.5 software was utilised to conduct preprocessing based on the Gauß algorithm. The acquired data were prepared and smoothed, followed by overlaying a cylindrical model onto each cell to locate its centre accurately. Subsequently, from these identified centres, a section was delineated per cell, targeting areas with minimal defects. These sections are presented in Figure A2 in Appendix A. The grey scale values along the delineated radial sections were extracted and exported for subsequent analysis using MATLAB R2022a. In the script, the imported data, containing position and grey scale values, representing the X-ray beam attenuation to the body, were subjected to a moving average filter to further mitigate noise. Fourier transformation was subsequently applied to the smoothed data to identify the frequency components. Peaks and troughs, signifying maxima and minima, respectively, were discerned in the Fourier-transformed data. The results are shown in Figure 3.

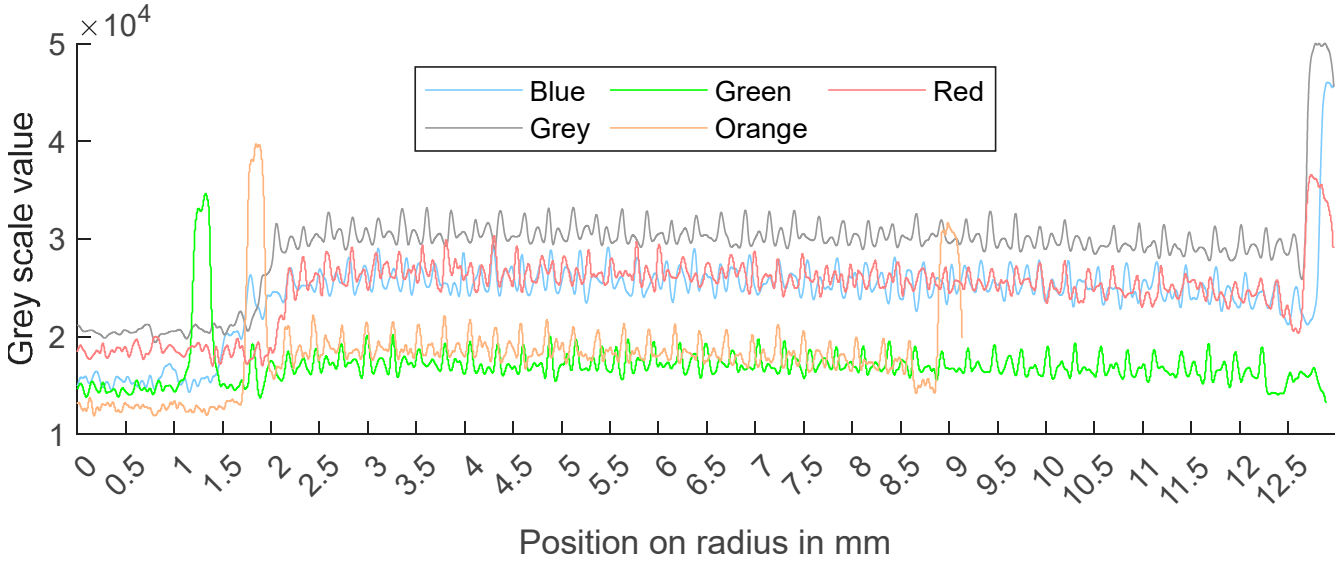

Figure 3. Overview of grey scale values over radii of the scanned cells.

Up to a radius of 2 cm, all cells showed minor variations apart from the pins of the green and orange cells. These are represented by a notable peak at a radius of 13.3 mm

for the green cell and 18.6 mm for the orange cell. From approximately 18–22 mm to the respective outer radii of 90 and 13 mm, a distinct zigzag pattern was observed, representing the jelly roll layers. This pattern was consistently observed across the jelly roll section with few irregularities. Due to the symmetry of the pattern, it can be assumed that the coatings of the current collector are homogeneous. The electrodes are distinguishable as minima and maxima within this pattern, although the separator does not appear to be clearly delineated. The orange cell also shows a peak at 8.99 mm, corresponding to its cell can. The grey, blue, and red cells exhibit a peak at the outer edge at 12.7–12.96 mm, which corresponds to the cell can, while the green cell lacks a similar peak. The reason for this remains unclear, but it can also be observed in the colouring of the cell can in Figure 2. The effective length of the jelly roll section is circa 10.62 mm (red) with 43 windings, 10.81 mm (green) with 39 windings, 6.99 mm (orange) with 6.99 windings, and 10.91 mm (blue) with 42 windings, 10.59 mm (grey) with 36 windings resulting in an average thickness per jelly roll layer of 259.8 µm (red), 277.2 µm (green), 268.8 µm (orange), 259,8 µm (blue), and 294.2 µm (grey). After identifying the design features and inhomogeneities without finding critical inconsistencies, the cells were electrically tested and then opened to gain precise geometrical information on the jelly roll, cell cap, and the lower cell.

2.6. Tear-Down of the Cells

The cells were opened in a MBraun glovebox filled with argon (pressure 2.5 mbar, 9.0 ppm H_2O, 3.7 ppm O_2) to maintain an inert atmosphere. The cells were transferred into and out of the glovebox through an airlock. Each cell was weighed individually inside the glove box with the masses listed in Table 2. The tear-down process involved four steps: cutting both ends of the cell open, severing the electrical contacts, removing the jelly roll, and unrolling the jelly roll. Regarding the materials, only one unexpected observation was made. As anticipated, the cells were encased in coloured polymer wraps and underneath, the cans and cell caps were metallic. Also, no variation in the case material for the green cell was observed, which might have been inferred from the different grey scale in the CT. It was observed that a substantial quantity of electrolyte was released upon opening the grey and red cells. Jelly roll composition comprised a graphite coating on both sides of a copper sheet for the anode, a white polymer separator, and an LFP coating on both sides of an aluminium sheet for the cathode. Apart from the red cell, both current collector sheets had tabs attached from the respective material. For the red cell, both tabs exhibited an aluminium appearance, despite the current collector being fabricated from copper. All insulators were made from either coloured or transparent polymer. No deviation was visible for the low-temperature cell.

Besides the thickness from each element, its specific properties are also relevant. From a material science perspective, it is reasonable to conclude that to support high discharge rates, the current collector and tabs of the anode should be constructed from copper, which possesses an electrical conductivity higher than nickel and slightly below that of silver, the element with the highest conductivity [44]. The rationale for the aluminium tabs welded on the copper current collector of the red cell remains unclear and necessitates electrical testing to evaluate its efficacy. The coatings were not analysed with respect to their chemical composition; however, as described in Chapter 3.2, laser scans were conducted to reveal the different particle sizes. The metallic material of the casing and cap, presumably steel, is a logical choice as it ensures the mechanical integrity of the battery cell while addressing cost and weight considerations. Insulators and separators appear similar across all five cells and are likely to conform to industry standards.

As presented in Figure 4 for the grey and orange cells, the bottom and top were disassembled, showing the cell isolations at cell bottom, the pin for the orange cell, can

fragments, and the design of the cut-open cell tops. CT views on both cell tops are presented in Figure A7 in Appendix A. The insights on the cell tops were used for deriving a CAD model providing the reference 18650 and 26650 models. A detailed evaluation of the electrodes is presented in the next section. No conceptual differences were identified among the separators of the cells.

Subsequently, the electrodes and separators were measured using a micrometre. Portions of the electrodes were then cut, either with the coating already detached or scraped off. The 26650-green and 18650-orange coatings stuck to the current collector and were barely removable. These cutouts were analysed using a Keyence VK-X250K confocal laser-scanning microscope. A 10× magnification was used to determine the coating thickness, while a 150× magnification was employed to examine the coating surface. The results of the scanning process steps are presented in Figures 5, A3, A4 and A6 in the Appendix A. The cathode coating varied more than 5 µm for the anode and more than 1 µm for the cathode coating.

Figure 4. Photographs of teared-down orange (**left**) and grey (**right**) cell without jelly roll.

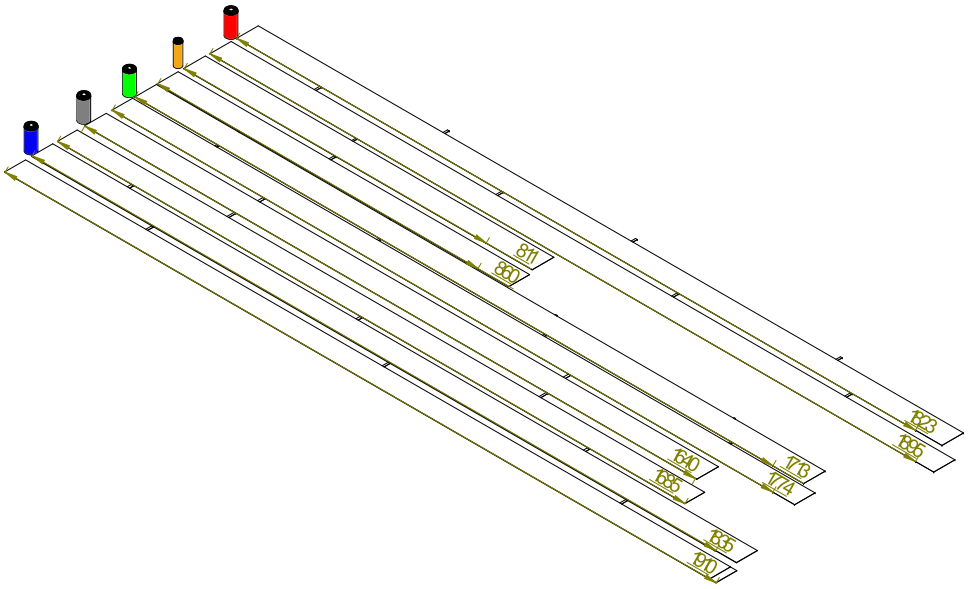

Figure 5. Comparison of the unrolled jelly rolls (measurement in mm).

3. Results and Discussion

3.1. Analysis of Cell Designs and Geometry

Based on the measurements, the main dimensions of the jelly roll and its specifics were derived. The main dimensions are presented in Table 3.

Table 3. Main dimensions of the jelly roll components: length (and width) in mm.

Cell	Blue	Grey	Orange	Red	Green
Cathode	1835 (56)	1640 (53)	811 (56)	1823 (57)	1713 (55)
Separator A	1890 (58)	1640 (58)	940 (58)	1900 (57)	1800 (58)
Anode	1910 (56)	1685 (53)	860 (56)	1895 (57)	1774 (55)
Separator B	1890 (58)	1690 (58)	940 (58)	1940 (57)	1830 (58)

The lengths of the anode and cathode components exhibit a consistent pattern across all cell types, with the anode always being slightly longer than the cathode. For the 26650 cells (blue, grey, red, and green), the cathode lengths range from 1640 mm to 1835 mm, while the anode lengths are between 1685 mm and 1910 mm, resulting in a 45–75 mm difference. Similarly, in the orange 18650 cell, the cathode measures 811 mm, and the anode is 860 mm long, reflecting a difference of 49 mm. The longer anode likely intended to ensure full electrochemical coverage during operation.

In all cases, the cathode and anode share the same width within each cell type, while the separator components are typically slightly wider. For the 26650 cells, the widths of the cathode and anode range from 53 mm to 57 mm, with separator widths of 58 mm, except for the red cell, where the separator matches the width of the electrodes at 57 mm. The orange 18650 cell follows the same pattern as the blue, grey, and green, with the cathode and anode both 56 mm wide, and the separators wider at 58 mm.

The comparison of the unrolled jelly rolls is presented in Figure 5. For each cell, the anode and cathode are displayed and each electrode's length is reported. Pictures from the teared-down cells are also presented in Figure A9 in the Appendix A. The jelly rolls exhibit distinct differences regarding tab concepts, cutout design, and tab dimensions across all examined cells.

For the red cell, the tab spacing ranges from 472 to 488 mm, with moderate cutout sizes and average tab dimensions (width of 5 mm, depth of 40 mm, and overhang 13–15 mm). It must also be noted that, for red, the positive and negative tabs have the highest distance to each other. The green cell features relatively smaller tab spacings (405–499 mm), minimal cutout dimensions (width 6–7 mm, depth 7–8 mm), and the smallest tabs (width 4–5 mm, depth 6 mm, and overhang 5 mm). The orange cell differs from the green cell from the same manufacturer and has unique design characteristics with only one tab per electrode, large cutouts (width 10 mm, depth 10–12 mm), and smaller tabs (width 4–5 mm, depth 7–6 mm). The blue cell displays moderate tab spacings (614–638 mm), larger cutouts (width of 9 mm, depth of 55–57 mm), and tabs with average dimensions (width of 6 mm, depth of 47 mm, and overhang of 11 mm). Also, the anode is longer than its separator. Despite being from the same manufacturer as blue, grey shows the largest tab spacings (821–838 mm), the largest cutouts (width of 10 mm, depth of 56–59 mm), and the largest tabs (width of 6 mm, depth of 53 mm, and overhang of 19 mm).

It is noteworthy that the grey cells consistently exhibit larger dimensions in spacing, cutouts, and tabs compared to the other cells. Green has the smallest cutout dimensions and tab sizes, whereas orange stands out owing to its single-tab design. Regarding the size and spacing, blue is dimensioned between the other configurations, whereas red represents an average size profile with the smallest spacing. These patterns highlight the variation in design philosophy and functional considerations among manufacturers.

No clear rule can be derived, but it is apparent that the grey cells' larger dimensions and opposing two taps are not derived from the three staggered blue cell tabs. For the green and orange cells, it is also apparent that those are different configurations with orange as the simplest design featuring only two tabs for both electrodes. It should also be noted that the orange tab design supports only approximately 42% of the maximum pulse discharge current compared to green.

The connections of the jelly rolls are designed differently. Except for orange and grey, the tabs are staggered. The orange cell uses a single-tab design, grey has two tabs, blue has three tabs, red has three tabs for the cathode plus four tabs for the anode, and green uses a four-tab design.

The analyses presented in Figure A8 in Appendix A show the anode overhang of the five cells, referring to the portion of the anode that extends beyond the edge of the separator, to provide an indicator of manufacturing quality. The blue cell exhibited minimal to no overhang in certain areas with an inhomogeneous and wavy pattern. The overhang varied significantly, ranging from almost no overhang to approximately 0.4 mm in length. In contrast, the grey cell had a long and homogeneous overhang, measuring consistently around 1.3 mm with a slight reduction towards the inner side. The green cell showed a medium overhang with an inhomogeneous and wavy pattern, ranging from approximately 0.3–1.3 mm. The orange cell presented a medium and consistent overhang of approximately 1 mm. Comparing the patterns of the orange and green cells, the consistency of the anode overhang is independent from the deployment of a pin. The red cell also had a medium overhang, varying from approximately 0.6–1.1 mm, with a slight wave near the outer region. The wavy anode overhang of the red cell explains the dark shades shown in Figure 2. From these observations, it can be concluded that cells with more homogeneous overhangs, such as grey and orange cells, may indicate a more stable manufacturing process and potentially better performance in terms of safety and longevity. The variability in the overhang, particularly in the blue and green cells, suggests potential inconsistencies in the production process that could affect cell performance and durability.

3.2. Thicknesses of Main Components

Deviations between the CT scan results of pristine cells and tear-down measurements after usage can be identified and probably arise from the inherent limitations of each method. Comparing both measurement results, the blue cell exhibited a relative decrease of −12% (from an average jelly roll thickness of 259.8 µm to a bottom-up calculation of 231.99 µm), while the grey, orange, red, and green cells displayed positive deviations of 18.9%, 9.4%, 22.4%, and 20.8%, respectively. This variation in sign suggests that the discrepancies are not due to uniform extension or contraction of cell components but rather due to limitations in resolution and accuracy of the measurement techniques.

CT scanning, though valuable for detecting gross inconsistencies and defects prior to cell usage, has limitations in maintaining internal accuracy. Variations in scanner properties during the scanning process and difficulties interpreting grey scale values, which are resolution-dependent, likely contributed to the discrepancies observed. Additionally, after tear-down, performing a full 3D scan of the entire jelly roll is impractical, necessitating the examination of smaller selected snippets. These snippets exhibited significant variance in the range of 1 to 5 µm in coating thickness, further complicating the accurate representation of the entire roll.

Thus, both CT scans and tear-down results are presented as complementary data points, each providing indicative values. These results serve as useful comparative references for other studies and can ultimately be incorporated into a simplified baseline model for further analysis.

In Figure 6, the results of the measurement during tear-down using the micrometre and 3D scan microscope after the electrical tests and scanning of pristine cells for the electrode coatings are presented. As expected, the high-power and low-temperature cells differ from the usually reported values probably mostly from energy cells. The thicknesses of the current collectors, cans, and tabs generally exceed the ranges specified in the published thicknesses. Specifically, the current collector anode and cathode thicknesses, as well as the tab thicknesses, were notably higher than the maximum values outlined in previous publications. Conversely, the coatings for the anode and cathode are thinner than those typically observed. However, the separator thicknesses are aligned with the published ranges, suggesting consistency with standard specifications. In the following, each cell element in Figure 6 is collated.

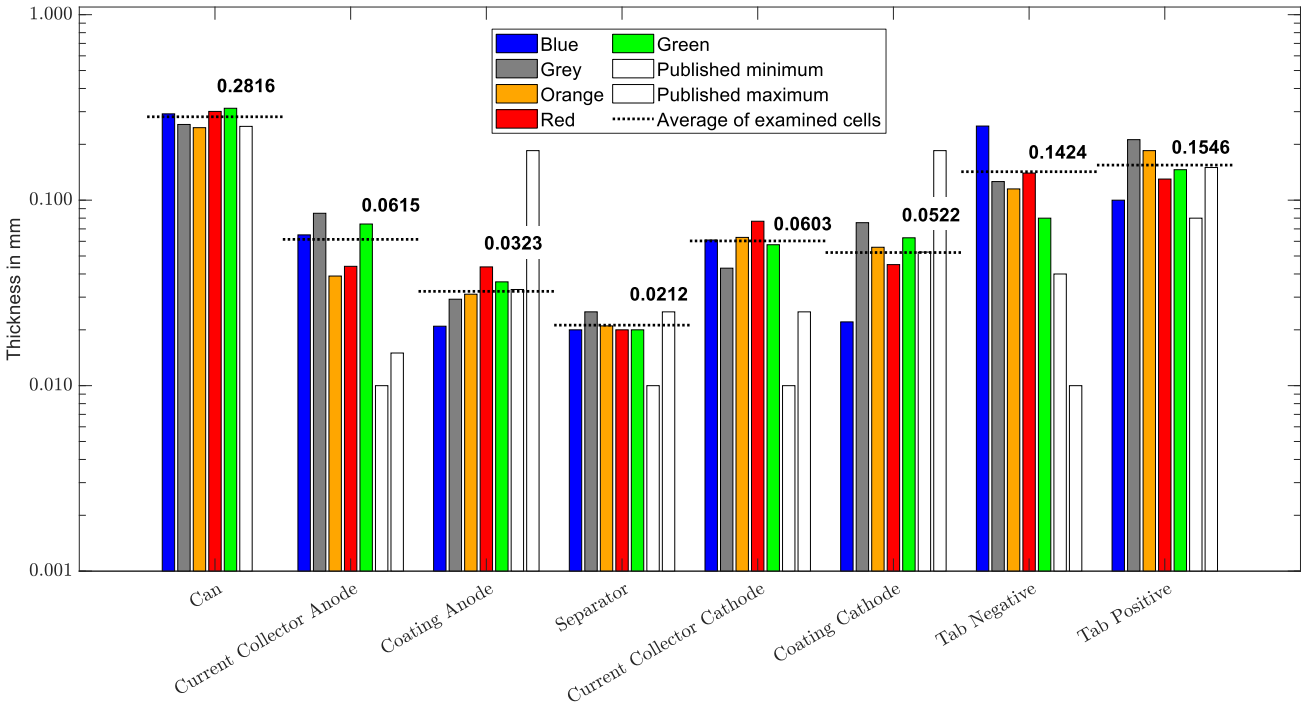

Figure 6. Comparison of measured thicknesses vs. the literature findings.

The wall thicknesses of the cell cans are 0.292 mm for blue, 0.256 mm for grey, 0.246 mm for orange, 0.301 mm for red, and 0.313 mm for green, resulting in an average of 0.28 mm (standard deviation of 0.026 mm). The published can thickness as shown in Table 1 is 0.25 mm. Besides the jelly roll, it must be noted that orange and green use a hollow pin with outer diameter of 3.2 mm and inner diameter of 2.8 mm to wrap up the jelly roll.

For the current collector of the anode, the blue cell has a wall thickness of 65 µm, grey of 85 µm, orange of 39 µm, red of 44 µm, and green of 74.4 µm. The average value of the examined cells is 61.48 µm (standard deviation of 17.66 µm). This average is 4.1 times higher than the published minimum of 15 µm and falls below the published maximum of 250 µm, indicating that the values are consistent with the published range but closer to the lower end.

In terms of the anode coating measured with the scanning microscope, blue has a thickness of 20.922 µm, grey of 29.247 µm, orange of 31.128 µm, red of 43.679 µm, and green of 36.279 µm. The average value for the examined cells is 32.251 µm (standard deviation of 7.52 µm). This average is less than 1 µm below the published minimum of 33 µm, suggesting that it is on the lower side of the published range.

For the separator, blue has a value of 20 µm, grey of 25 µm, orange of 21 µm, red of 20 µm, and green of 20 µm. The average value of the examined cells is 21.2 µm (standard deviation of 1.83 µm). This average is 2.12 times higher than the published minimum of 10 µm and 0.85 times below the published maximum of 25 µm, indicating that the values are within the range and closer to the minimum.

The current collector of the cathode has a thickness of 61 µm for the blue cell, 43 µm for the grey cell, 63 µm for the orange cell, 77 µm for the red cell, and 57.518 µm for the green cell. The average value of the cells examined was 60.3036 µm (standard deviation of 10.88 µm). This average is 6.03 times higher than the published minimum of 10 µm, and approximately 35 µm below the published maximum of 25 µm, indicating that the values are higher than the published range.

Regarding the coating of the cathode measured with the scanning microscope, blue has a thickness of 22.073 µm, grey of 75.632 µm, orange of 55.747 µm, red of 44.943 µm, and green of 62.688 µm. The average value of the examined cells is 52.2166 µm (standard deviation of 18.05 µm). This average is 0.48 times below the published minimum of 52.5 µm and well below the published maximum of 185 µm.

The negative tab thicknesses are 251, 126, 115, 140, and 80 µm for blue, grey, orange, red, and green, respectively. The average thickness of the cells examined is 142.4 µm (standard deviation of 57.94 µm). This average is 3.56 times higher than the published minimum of 40 µm and 1.42 times less than the published maximum of 150 µm, indicating that the values are fully within the range.

The positive tab thicknesses are 100, 212, 185, 130, and 146 µm for the blue, grey, orange, red, and green cells, respectively. The average thickness is 154.6 µm (standard deviation of 37.16 µm). This average is 1.93 times higher than the published minimum of 80 µm and less than 5 µm below the published maximum of 150 µm.

To further examine the different designs, the combination of the number of tabs, cell capacity, and coating thickness are presented in Figure 7 on the left. No consistent trend between the coating thickness and capacity or between the coating thickness and the number of tabs can be deduced. Cells with higher capacities tend to have more taps for their anodes and cathodes, apart from the grey cells. Comparing the 18650 vs. 26650 of Lithium Werks, the orange and green cells show that the coating thicknesses increased by 5.151 µm for the anode and 6.941 µm for the cathode. In addition, the anode and cathode use four tabs instead of one. Hence, it can be deducted that the 26650 is not an extended 18650, but its own design. Regarding the adjustments for low-temperature operations, the comparison of grey vs. blue from Wiltson show that the low-temperature application has 8.325 µm less coating for the anode and 53.559 µm for the cathode. Complementary to the additional tab, these differences also lead to the conclusion that the whole design and not only the chemistry was changed for the low-temperature application.

On the right-hand side in Figure 7, it is clearly discernible that both cells with the lowest operating temperature according to the data sheet utilise a minimal number of tabs. This may be attributed to an increased heating effect. However, it is important to consider that the data sheets might not define the boundary operating conditions for the temperature. This observation is further supported by a study in which the cell voltage only began to decrease after freezing below −100 °C [45]. Moreover, further investigation is necessary to ascertain how the tab configuration influences the capacity for pulses.

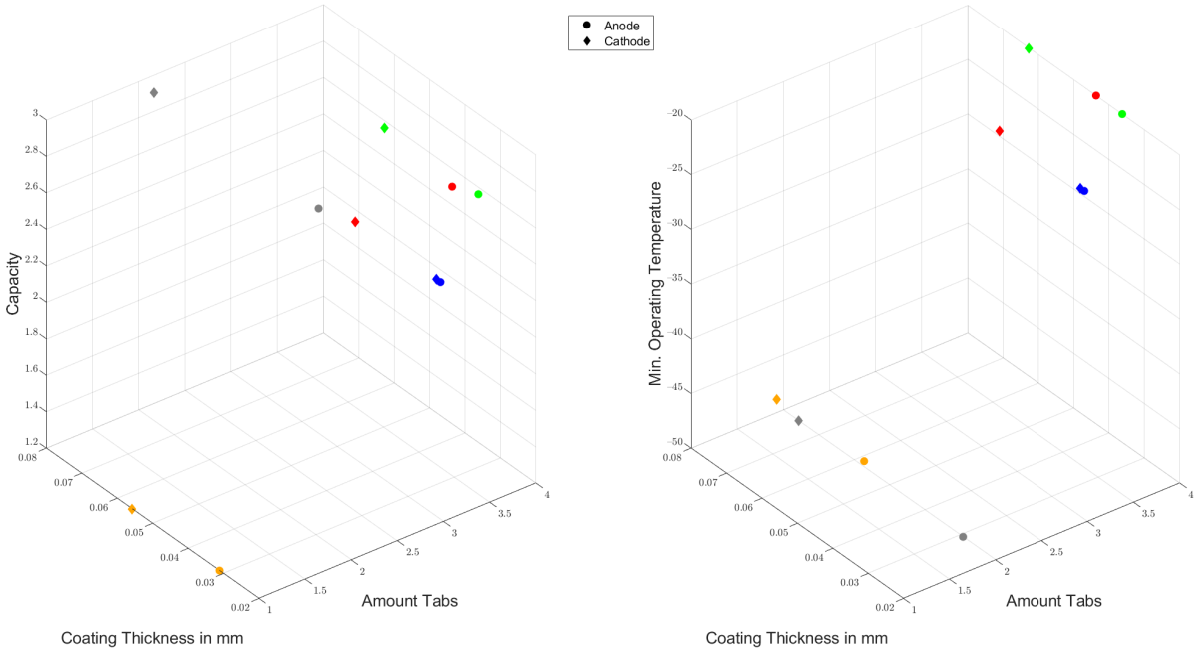

Figure 7. Evaluation tabs and coating thickness vs. capacity/temperature for all cells.

As presented in Figure 8, a correlation between configurations with a higher number of tabs (both positive and negative) and the ability to provide higher pulses, such as in the green cell, can be inferred. Conversely, configurations with fewer tabs, exemplified by the orange and grey cells, exhibit lower maximum pulse currents and demonstrate higher impedance. Consequently, a trade-off between the ability to operate at low temperatures and provide high pulses is evident.

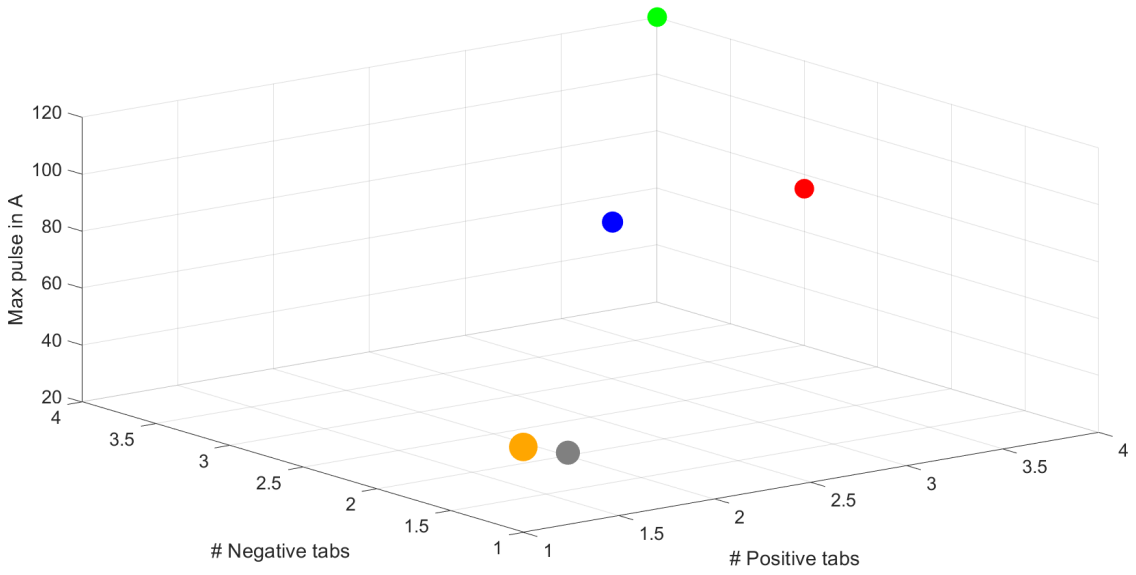

Figure 8. Dependency of max pulse and number of tabs (with marker size related to impedance).

To examine geometrical effects on the cell impedance, four additional analyses were performed as presented in Figure 9 with focus on the anode aspects.

Firstly, the average particle size of the anode was examined as a potential factor. The anode surface exploration images from the laser scan microscope (Figure A6) were analysed using ImageJ to compare the average particle size. Although no clear pattern could be derived, smaller particles appeared to correspond with lower cell impedance. This observation is

supported by a study on the improvement of low-temperature cell performance [32]. Secondly, the thickness of the anode current collector exhibited a plateau effect. The thinnest current collector (orange) demonstrated the highest impedance, while the thickest (grey) showed the second-highest impedance. This suggests that the lower resistance of a thicker current collector is counterbalanced by other factors. Therefore, the coating on the current collector and the overall cross-section need to be analysed. Thirdly, no discernible pattern was observed in relation to the thickness of the coating anode, as the data points were scattered with no clear increase or decrease in impedance values. Fourthly, the cross-sectional area of the negative tabs multiplied by the number of tabs was examined. While no clear pattern emerged, the impedance appeared to correlate with the negative tab area.

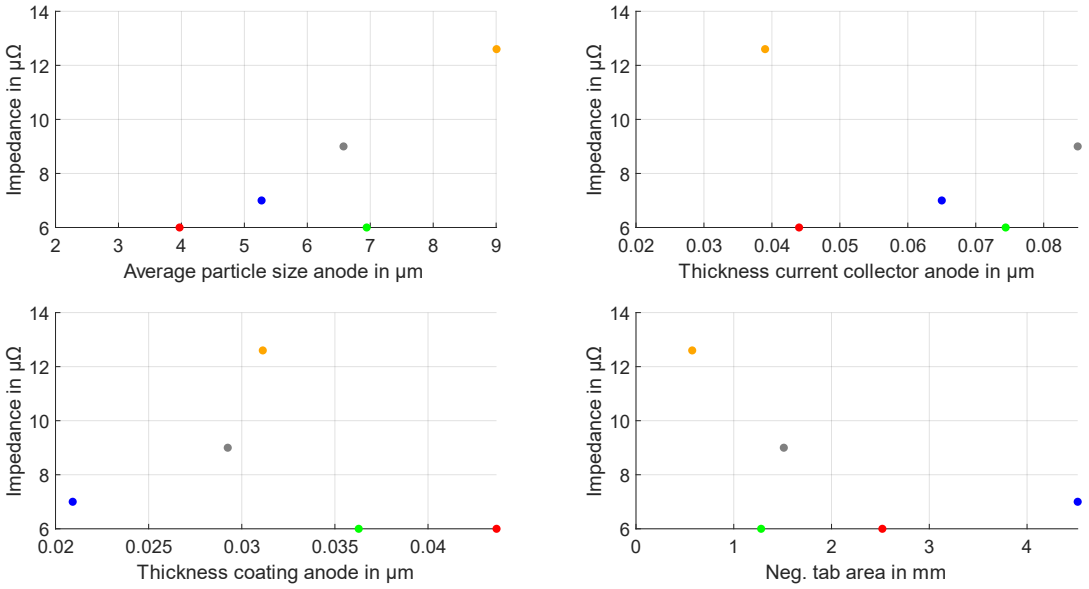

Figure 9. Evaluation of impedance.

For all four findings, it must be considered that the material choice and specific properties, such as conductivity, likely have a significant influence. Additionally, it is possible that certain thresholds may alter the dependency of the impedance (for example, a larger tab area may become less relevant once it reaches a sufficient size).

3.3. Deviated Reference Model of 18650 and 26650 High-Power Cells

Based on the presented findings, two reference models were derived as a 3D representation of the main features The process of generating battery cell models for 18650 and 26650 cells was carried out using a combination of Synera and Siemens NX. Initially, the components and their specific characteristics were defined to ensure an adequate representation of the cell geometry. A parameterized cell top was designed based on the findings for both cell formats. Subsequently, additional elements such as the housing and insulation components were constructed. To model the jelly roll, an incremental logic was developed, enabling the successive layering of the jelly roll along a spiral path until it reached the interior can surface. Finally, the complete model was exported in STP format, facilitating its integration into virtual experiments such as finite element analysis.

For further proceedings, simplifications were assumed. The derived models have a spiral-shaped jelly roll without space between the layers or deformation owing to the taps and homogeneous wall thicknesses. As a quality check, the number of windings for the jelly roll of the CAD models were compared with the investigated range of the examined cells. In addition to the jelly roll, the design of the cell top with the safety mechanism was generated according to the researched patent and detailed views from the CT scans. The safety vent

was designed to rupture if a critical internal pressure occurs, and the current interrupting device was designed to bend and physically disconnect the electrical connection in critical cases of pressure. A central pin was designed with a 1.5 mm radius and 0.2 mm thickness. The length and diameter of the jelly roll were set without tolerances and overhangs to 59.7 mm and a centrally aligned pin with a length of 53 mm. The cell top was designed as shown in Figure 1. Also, a 0.2 mm insulator disc was added to the bottom to avoid contact with the bottom. The tab connections were not designed as the amount and positioning of tabs needed to be adjusted for each use case. Regarding the design of the jelly rolls the 18650 and the 26650 were differentiated. Both models are publicly accessible and stored on Zenodo, an open-access repository for research outputs under the following links: https://zenodo.org/records/14680279?token=eyJhbGciOiJIUzUxMiJ9.eyJpZCI6Ijc5ODY1MGM5LTM1NGMtNDQyOS1hNjFiLTUxYjk2Y2MwZmE1NCIsImRhdGEiOnt9LCJyYW5kb20iOiJkZTNlY2Y0ZmQ5OWUyZjgxMWE2ODRhODQ4NTUwNGIxNyJ9.WkzrRUi43UHAp6qF6KxRtRSjs7xHRUug139bjz7N0P3HVi-zTlyjxFmXQm (accessed 17 January 2025) and https://zenodo.org/records/14680248?token=eyJhbGciOiJIUzUxMiJ9.eyJpZCI6ImI3YmVlYmQ0LTljZDUtNDdmOC1iZTAzLWFmOTM2YmJmYTg2YSIsImRhdGEiOnt9LCJyYW5kb20iOiJkMGJmZWJkYzQxY2ZiNjJiNzI5ODkxNzY0NmIzMTRkYSJ9.mteE4-z-tNfDI__IZwNbyegtFXgffSPzwLLQ8WLg728FWNKL66vehuqc12 (accessed 17 January 2025). A sketch of both cells is presented in Figure 10.

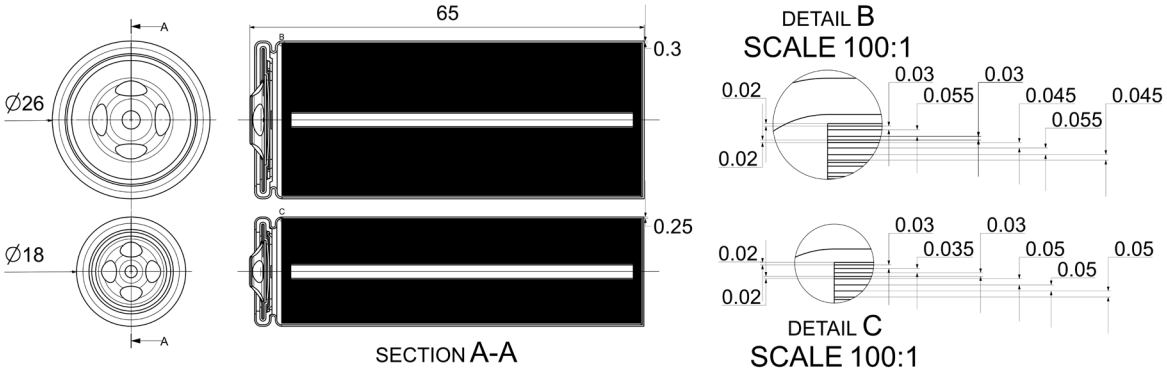

Figure 10. Sketch of both cell models.

The model for the 18650 power cells has a simplified wall thickness of 35 µm for the current collector anode, 30 µm for the anode coating, 20 µm for the separator, 50 µm for the current collector cathode, 50 µm for the cathode coating, and 0.25 mm for the can. Also, no thickness deviations of jelly roll layers are considered, resulting in 814.604 mm anode length (in comparison to 860 mm for the orange cell).

The 26650 power cells have a simplified wall thickness of 55 µm for the current collector anode, 30 µm for the anode coating, 20 µm for the separator, 55 µm for the current collector cathode, 45 µm for the cathode coating, and 0.30 mm for the can is assumed. Also, no thickness deviations of jelly roll layers are considered, resulting in a 1659.860 mm anode length (in comparison to 1685–1910 mm for the 26650 cells).

4. Conclusions

Although publications based on CT and postmortem analysis of cells and cell components have been conducted previously, the elaborated results confirmed that the coating thicknesses for high-power cells are thinner than most previously published data, whereas the separators and cans correspond to the published values. Conversely, current collectors and tabs appear to be relatively thick for high-power and low-temperature applications. These findings support the hypothesis that typically, high-energy cells are not examined.

The anode coating thickness averaged 32.25 µm (20.92–43.68 µm), marginally below the published minimum of 33 µm. Cathode coatings averaged 52.21 µm (22.07–75.63 µm), slightly below the minimum of 52.5 µm. Anode current collectors averaged 61.48 µm (39–85 µm), significantly above the published maximum of 15 µm, while cathode current collectors averaged 60.30 µm (43–77 µm), considerably above the reference of 25 µm. The can wall thickness averaged 0.41 mm (0.30–0.50 mm), consistent with the literature values. Anode tabs averaged 142.4 µm (80–251 µm), below the published maximum of 150 µm, while cathode tabs averaged 154.6 µm (100–212 µm), marginally exceeding the maximum. It was found that smaller particles of the anode coating reduce the cell's impedance and that the cell's configuration needs to balance the ability to be operated at low temperatures versus the ability to provide high pulses.

It should be noted that no general approach regarding the number (1–4) and distribution of tabs was deduced, and diverse concepts for the cell tops were observed. In conclusion, aside from the comparison with prior published data, no significant similarities were observed concerning configuration and thicknesses across the five cell types analysed. While a plausible geometry for 18650 and 26650 high-power cells was derived, there is no evidence suggesting that manufacturers scale their cells from 18650 to 26650 or make solely chemical adjustments to adapt existing cells for low-temperature applications. The findings indicate that, in both cases, the configuration and geometry were distinctly chosen, reflecting different design considerations rather than a straightforward scaling or chemical modification approach, thus disproving those hypotheses.

Based on the presented findings for the LFP cells, this paper suggests verifying the data sheets regarding the electrical performance, such as pulses and suitability for low-temperature applications, to derive insights on the real impact of the identified design differences. Additionally, the chemical effects should be included. The provided CAD models may be utilised for further virtual analyses of different cell geometries or material properties.

Author Contributions: Conceptualization, F.W.; methodology, F.W. and A.S.; software, F.W.; validation, F.W.; formal analysis, F.W.; investigation, F.W. and A.S.; data curation, F.W. and M.L.; writing—original draft preparation, F.W.; writing—review and editing, F.W., A.S., and J.K.; visualisation, F.W. and M.L.; project administration, F.W.; funding acquisition, F.W. All authors have read and agreed to the published version of the manuscript.

Funding: This research was funded by the IBB Business Team GmbH and was further supported by the German Research Foundation and the Open Access Publication Fund of TU Berlin.

Institutional Review Board Statement: Not applicable.

Informed Consent Statement: Not applicable.

Data Availability Statement: The original contributions presented in the study are included in the article, further inquiries can be directed to the corresponding author/s.

Acknowledgments: Gratitude is extended to Stefan Wätzold of the Stefan Wätzold Projekt GmbH for his invaluable support throughout this project. Appreciation is also due to Joachim Weinhold and the Zentraleinrichtung 3D Technologien for their technical expertise and assistance. Sincere thanks go to Kristin Mahlow of the Museum für Naturkunde Berlin for her collaboration and the usage of their CT. Thanks is owed to the team and especially Tobais Wigand from Synera for supporting the modellation process. Finally, acknowledgment is given to Pascal Pinter of Hexagon AB for providing valuable insights into Volumegraphics and handling the CT data. We acknowledge support by the German Research Foundation and the Open Access Publication Fund of TU Berlin.

Conflicts of Interest: Author Florian Wätzold was employed by the company Stefan Wätzold Projekt GmbH. The remaining authors declare that the research was conducted in the absence of any commercial or financial relationships that could be construed as a potential conflict of interest.

Appendix A

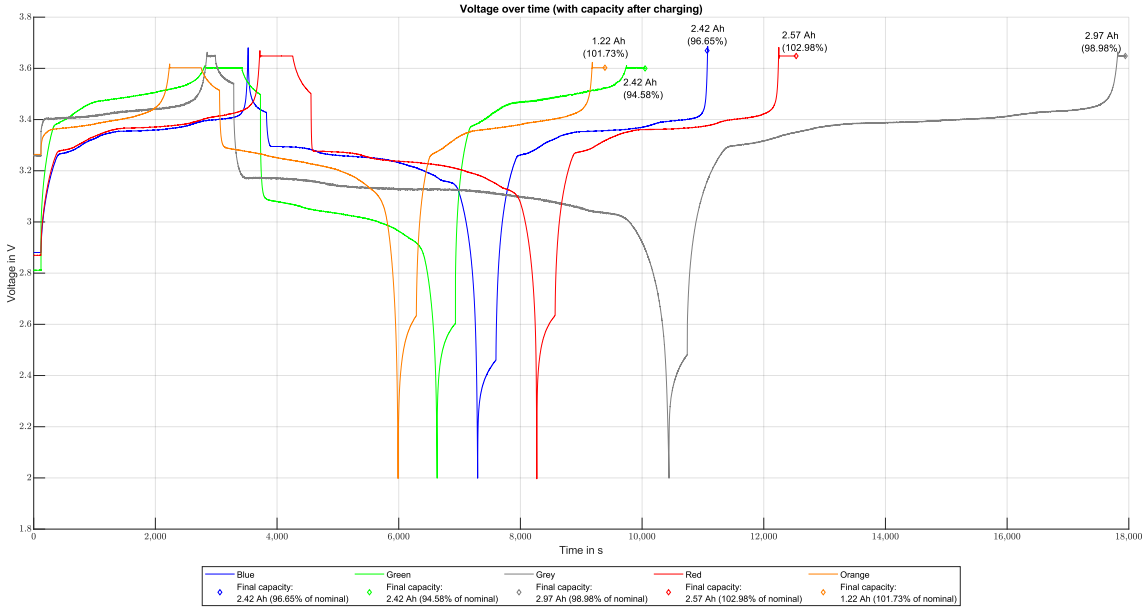

Figure A1. Capacity of cells after initial discharge and charge.

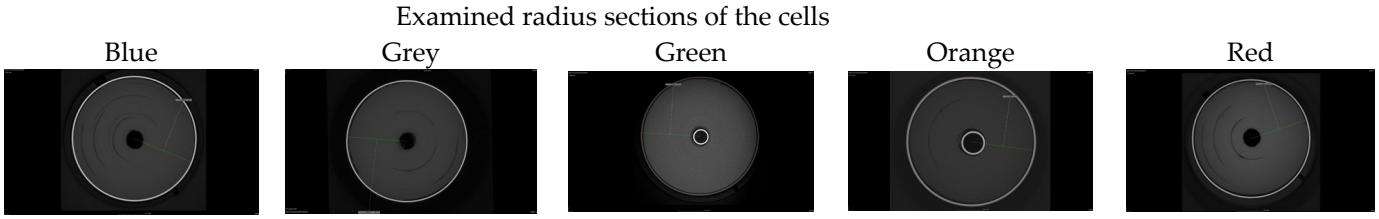

Figure A2. CT sections for analysis.

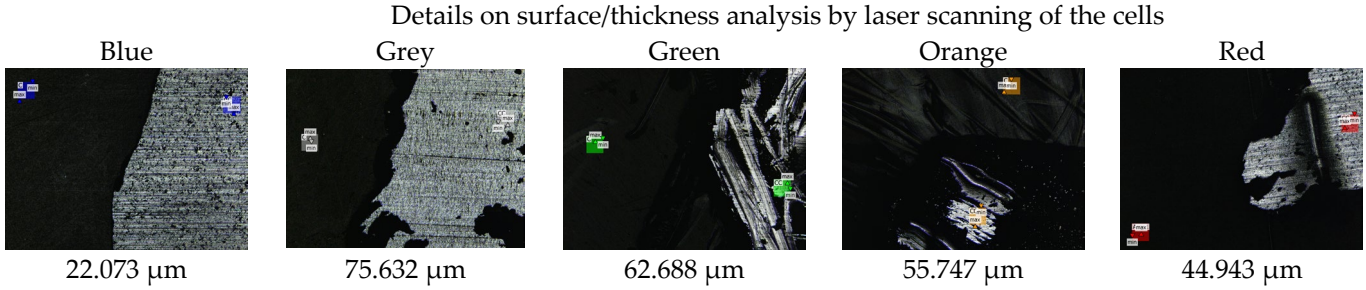

Figure A3. Evaluation thickness/height difference of current collector to cathodecoating.

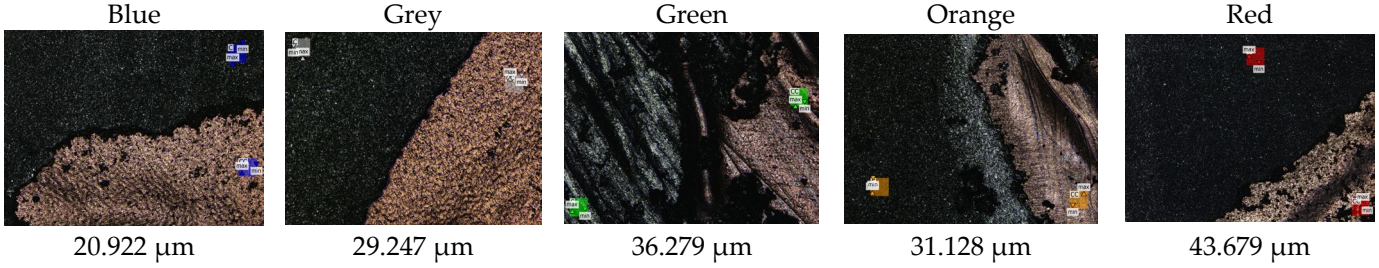

Figure A4. Evaluation thickness/height difference of current collector to anode coating.

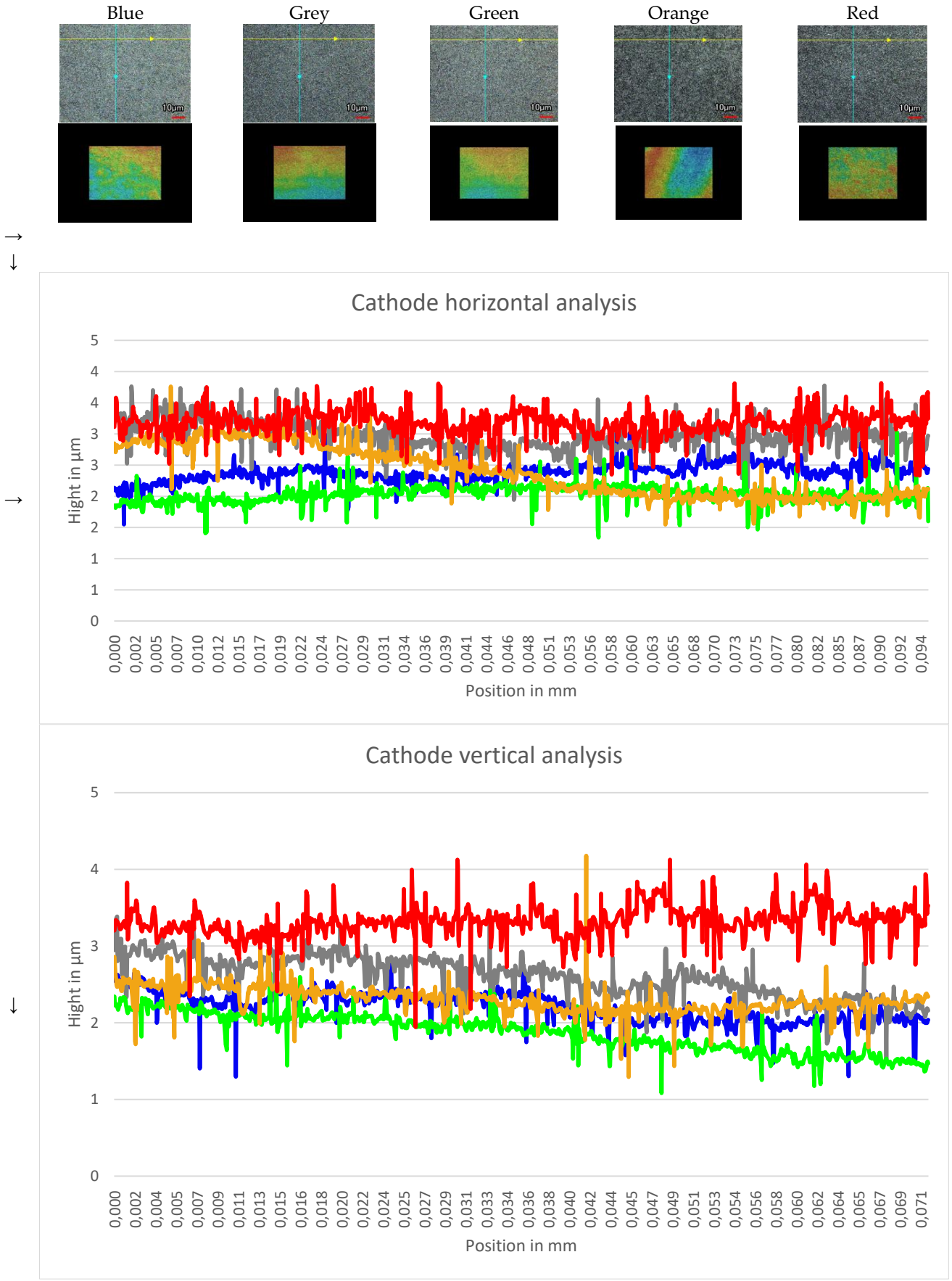

Figure A5. Evaluation surface cathode coating.

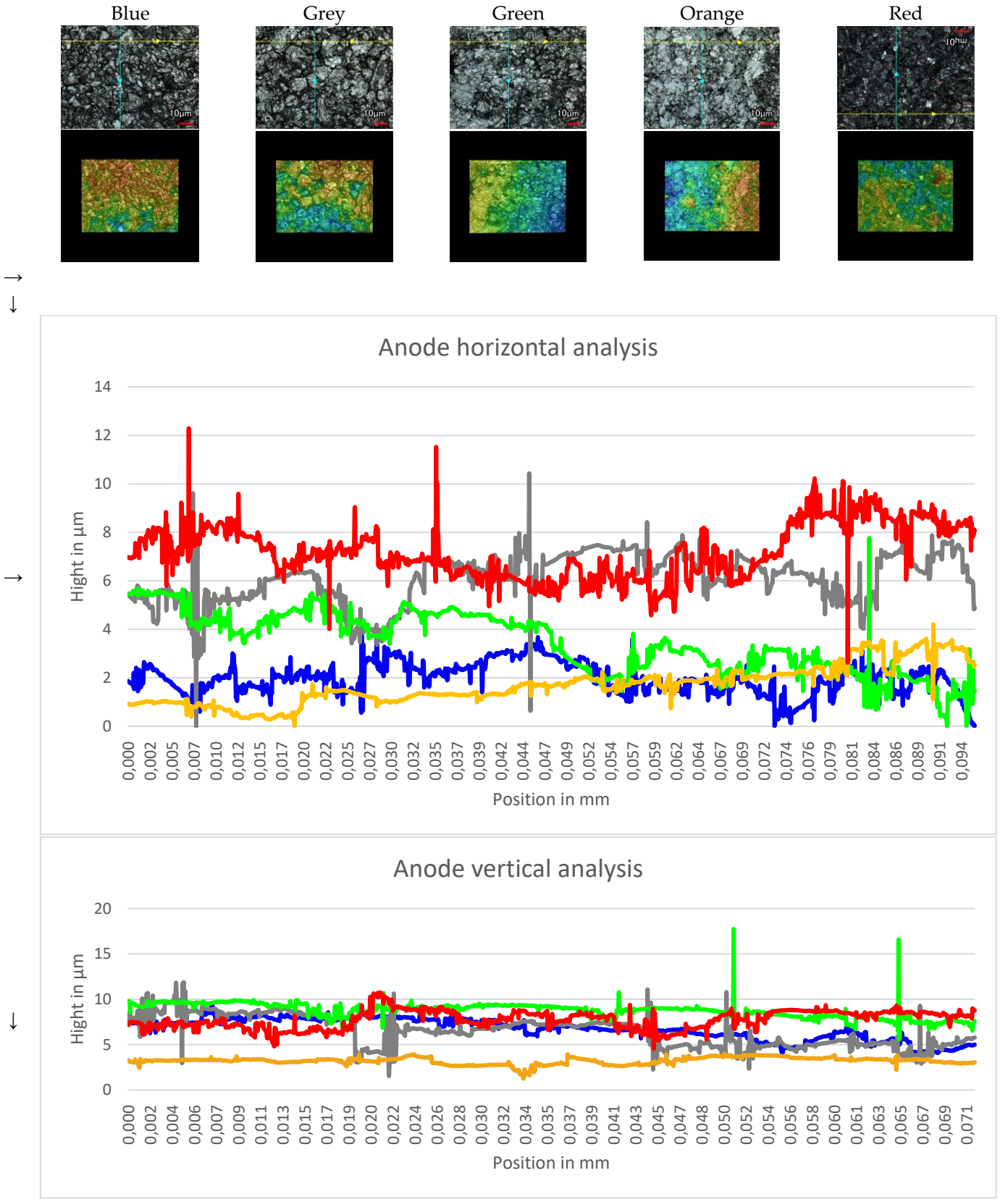

Figure A6. Evaluation surface anode coating.

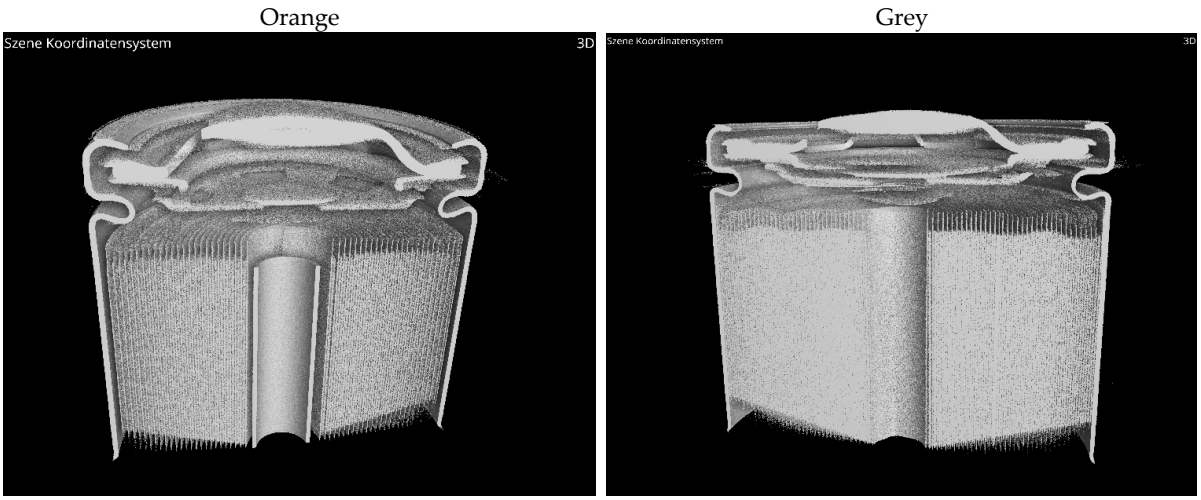

Figure A7. CT details of orange and grey cell tops.

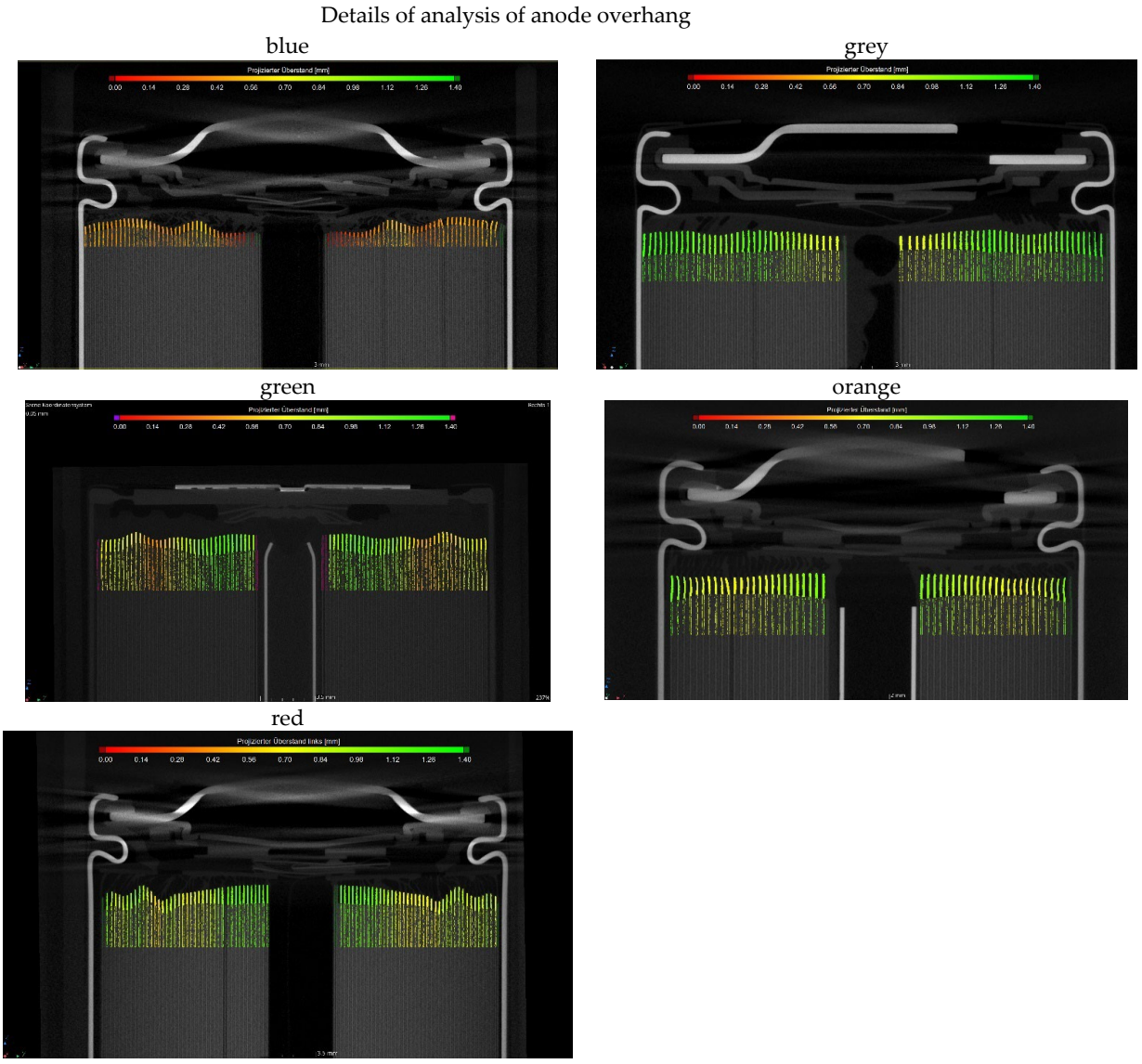

Figure A8. Analysis of anode overhang as projected overhang.

Figure A9. Detail pictures from cell tear-down.

References

1. Rahimzei, E. *Kompendium: Li-Ionen-Batterien: Im BMWi Förderprogramm IKT Für Elektromobilität II: Smart Car—Smart Grid—Smart Traffic*; VDE: Frankfurt am Main, Germany, 2015.
2. Waldmann, T.; Scurtu, R.-G.; Richter, K.; Wohlfahrt-Mehrens, M. 18650 vs. 21700 Li-Ion Cells—A Direct Comparison of Electrochemical, Thermal, and Geometrical Properties. *J. Power Sources* **2020**, *472*, 228614. [CrossRef]
3. Baazouzi, S.; Feistel, N.; Wanner, J.; Landwehr, I.; Fill, A.; Birke, K.P. Design, Properties, and Manufacturing of Cylindrical Li-Ion Battery Cells—A Generic Overview. *Batteries* **2023**, *9*, 309. [CrossRef]
4. BMW Future Batteries. Available online: https://www.sae.org/site/news/2023/01/bmw-future-batteries---ulrich (accessed on 26 October 2024).
5. Primary Batteries General; Revision Underway. 2022. Available online: https://www.en-standard.eu/bs-en-iec-60086-1-2021-primary-batteries-general/ (accessed on 15 January 2025).
6. Kurzweil, P.; Dietlmeier, O.K. *Elektrochemische Speicher*; Springer Fachmedien Wiesbaden: Wiesbaden, Germany, 2018; ISBN 978-3-658-21828-7.
7. Li, F.; Tao, R.; Tan, X.; Xu, J.; Kong, D.; Shen, L.; Mo, R.; Li, J.; Lu, Y. Graphite-Embedded Lithium Iron Phosphate for High-Power–Energy Cathodes. *Nano Lett.* **2021**, *21*, 2572–2579. [CrossRef] [PubMed]
8. Zhuang, W.; Lu, S.; Lu, H. Progress in Materials for Lithium-Ion Power Batteries. In Proceedings of the 2014 International Conference on Intelligent Green Building and Smart Grid (IGBSG), Taipei, Taiwan, 23–25 April 2014; pp. 1–2.
9. Wu, Y.; Huang, X.; Huang, L.; Chen, J. Strategies for Rational Design of High-Power Lithium-ion Batteries. *Energy Env. Mater.* **2021**, *4*, 19–45. [CrossRef]
10. Worku, B.E.; Zheng, S.; Wang, B. Review of Low-temperature Lithium-ion Battery Progress: New Battery System Design Imperative. *Int. J. Energy Res.* **2022**, *46*, 14609–14626. [CrossRef]

11. Wätzold, F.; Dahm, H.-P.; Binder, J.; Standfest, J. Leichtbaubewertung von Starterbatterien auf Lithium-Basis. *ATZ-Automobiltech. Z.* **2021**, *123*, 60–65. [CrossRef]
12. Bauknecht, S.; Wätzold, F.; Schlösser, A.; Kowal, J. Comparing the Cold-Cranking Performance of Lead-Acid and Lithium Iron Phosphate Batteries at Temperatures below 0 °C. *Batteries* **2023**, *9*, 176. [CrossRef]
13. How the Climatic Wind Tunnel in Weissach Works. Available online: https://newsroom.porsche.com/en/2024/innovation/porsche-simulating-climate-conditions-climatic-wind-tunnel-weissach-36348.html (accessed on 20 October 2024).
14. Wallentowitz, H.; Reif, K. (Eds.) *Handbuch Kraftfahrzeugelektronik: Grundlagen, Komponenten, Systeme, Anwendungen*; Auflage; Vieweg: Wiesbaden, Germany, 2006; ISBN 978-3-528-03971-4.
15. Ketterer, B.; Karl, U.; Möst, D.; Ulrich, S. *Lithium-Ionen Batterien: Stand Der Technik Und Anwendungspotential in Hybrid-, Plug-In Hybrid- Und Elektrofahrzeugen. Lithium-Ion Batteries: State of the Art and Application Potential in Hybrid-, Plug-in Hybrid- and Electric Vehicles*; Karlsruhe Institute of Technology: Karlsruhe, Germany, 2010.
16. Zhu, P.; Gastol, D.; Marshall, J.; Sommerville, R.; Goodship, V.; Kendrick, E. A Review of Current Collectors for Lithium-Ion Batteries. *J. Power Sources* **2021**, *485*, 229321. [CrossRef]
17. Lain, B. Kendrick Design Strategies for High Power vs. High Energy Lithium Ion Cells. *Batteries* **2019**, *5*, 64. [CrossRef]
18. Son, B.; Ryou, M.-H.; Choi, J.; Kim, S.-H.; Ko, J.M.; Lee, Y.M. Effect of Cathode/Anode Area Ratio on Electrochemical Performance of Lithium-Ion Batteries. *J. Power Sources* **2013**, *243*, 641–647. [CrossRef]
19. Tagawa, K.; Brodd, R.J. Production Processes for Fabrication of Lithium-Ion Batteries. In *Lithium-Ion Batteries*; Yoshio, M., Brodd, R.J., Kozawa, A., Eds.; Springer: New York, NY, USA, 2009; pp. 1–14. ISBN 978-0-387-34444-7.
20. Kim, S.; Lee, Y.S.; Lee, H.S.; Jin, H.L. A Study on the Behavior of a Cylindrical Type Li–Ion Secondary Battery under Abnormal Conditions. *Mater. Werkst.* **2010**, *41*, 378–385. [CrossRef]
21. Li, W.; Crompton, K.R.; Hacker, C.; Ostanek, J.K. Comparison of Current Interrupt Device and Vent Design for 18650 Format Lithium-Ion Battery Caps. *J. Energy Storage* **2020**, *32*, 101890. [CrossRef]
22. Willenberg, L.; Dechent, P.; Fuchs, G.; Teuber, M.; Eckert, M.; Graff, M.; Kürten, N.; Sauer, D.U.; Figgemeier, E. The Development of Jelly Roll Deformation in 18650 Lithium-Ion Batteries at Low State of Charge. *J. Electrochem. Soc.* **2020**, *167*, 120502. [CrossRef]
23. Wierzbicki, T.; Sahraei, E. Homogenized Mechanical Properties for the Jellyroll of Cylindrical Lithium-Ion Cells. *J. Power Sources* **2013**, *241*, 467–476. [CrossRef]
24. Ender, M.; Joos, J.; Weber, A.; Ivers-Tiffée, E. Anode Microstructures from High-Energy and High-Power Lithium-Ion Cylindrical Cells Obtained by X-Ray Nano-Tomography. *J. Power Sources* **2014**, *269*, 912–919. [CrossRef]
25. Quinn, J.B.; Waldmann, T.; Richter, K.; Kasper, M.; Wohlfahrt-Mehrens, M. Energy Density of Cylindrical Li-Ion Cells: A Comparison of Commercial 18650 to the 21700 Cells. *J. Electrochem. Soc.* **2018**, *165*, A3284–A3291. [CrossRef]
26. Pfrang, A.; Kersys, A.; Kriston, A.; Sauer, D.U.; Rahe, C.; Käbitz, S.; Figgemeier, E. Long-Term Cycling Induced Jelly Roll Deformation in Commercial 18650 Cells. *J. Power Sources* **2018**, *392*, 168–175. [CrossRef]
27. Orendorff, C.J. The Role of Separators in Lithium-Ion Cell Safety. *Interface Mag.* **2012**, *21*, 61–65. [CrossRef]
28. Zheng, H.; Li, J.; Song, X.; Liu, G.; Battaglia, V.S. A Comprehensive Understanding of Electrode Thickness Effects on the Electrochemical Performances of Li-Ion Battery Cathodes. *Electrochim. Acta* **2012**, *71*, 258–265. [CrossRef]
29. Li, D.; Lv, Q.; Zhang, C.; Zhou, W.; Guo, H.; Jiang, S.; Li, Z. The Effect of Electrode Thickness on the High-Current Discharge and Long-Term Cycle Performance of a Lithium-Ion Battery. *Batteries* **2022**, *8*, 101. [CrossRef]
30. Wang, J.; Yu, D.; Sun, X.; Wang, H.; Li, J. Anodes for Low-Temperature Rechargeable Batteries. *eScience* **2024**, *4*, 100252. [CrossRef]
31. Selinis, P.; Farmakis, F. Review—A Review on the Anode and Cathode Materials for Lithium-Ion Batteries with Improved Subzero Temperature Performance. *J. Electrochem. Soc.* **2022**, *169*, 010526. [CrossRef]
32. Zhan, J.; Deng, Y.; Ren, J.; Gao, Y.; Liu, Y.; Rao, S.; Li, W.; Gao, Z. Cell Design for Improving Low-Temperature Performance of Lithium-Ion Batteries for Electric Vehicles. *Batteries* **2023**, *9*, 373. [CrossRef]
33. Lee, K.-J.; Smith, K.; Pesaran, A.; Kim, G.-H. Three Dimensional Thermal-, Electrical-, and Electrochemical-Coupled Model for Cylindrical Wound Large Format Lithium-Ion Batteries. *J. Power Sources* **2013**, *241*, 20–32. [CrossRef]
34. Duan, Y.; Wu, H.; Huang, L.; Liu, L.; Zhang, Y. Optimizing Current Terminals of 18 650 Lithium-Ion Power Batteries under High Discharge Current. *Energy Technol.* **2017**, *5*, 1619–1626. [CrossRef]
35. Li, S.; Kirkaldy, N.; Zhang, C.; Gopalakrishnan, K.; Amietszajew, T.; Diaz, L.B.; Barreras, J.V.; Shams, M.; Hua, X.; Patel, Y.; et al. Optimal Cell Tab Design and Cooling Strategy for Cylindrical Lithium-Ion Batteries. *J. Power Sources* **2021**, *492*, 229594. [CrossRef]
36. Tranter, T.G.; Timms, R.; Shearing, P.R.; Brett, D.J.L. Communication—Prediction of Thermal Issues for Larger Format 4680 Cylindrical Cells and Their Mitigation with Enhanced Current Collection. *J. Electrochem. Soc.* **2020**, *167*, 160544. [CrossRef]
37. LG Chem, Ltd. *Zylinderförmige Wiederaufladbare Batterie*; LG Chem, Ltd.: Seoul, Republic of Korea, 2017.
38. VDI/VDE-Gesellschaft Mess- und Automatisierungstechnik. *Computed Tomography in Dimensional Measurement—Influencing Variables on Measurement Results and Recommendations for Computed Tomography Dimensional Measurements*; VDI/VDE-Gesellschaft Mess- und Automatisierungstechnik: Berlin-Charlottenburg, Germany, 2018.

39. Kok, M.D.R.; Robinson, J.B.; Weaving, J.S.; Jnawali, A.; Pham, M.; Iacoviello, F.; Brett, D.J.L.; Shearing, P.R. Virtual Unrolling of Spirally-Wound Lithium-Ion Cells for Correlative Degradation Studies and Predictive Fault Detection. *Sustain. Energy Fuels* **2019**, *3*, 2972–2976. [CrossRef]
40. Villarraga-Gómez, H.; Begun, D.L.; Bhattad, P.; Mo, K.; Norouzi Rad, M.; White, R.T.; Kelly, S.T. Assessing Rechargeable Batteries with 3D X-Ray Microscopy, Computed Tomography, and Nanotomography. *Nondestruct. Test. Eval.* **2022**, *37*, 519–535. [CrossRef]
41. Evaluation of Measurement Data—Guide to the Expression of Uncertainty in Measurement. 2008. Available online: https://www.bipm.org/documents/20126/2071204/JCGM_100_2008_E.pdf/cb0ef43f-baa5-11cf-3f85-4dcd86f77bd6 (accessed on 15 January 2025).
42. Chen, C.-H.; Brosa Planella, F.; O'Regan, K.; Gastol, D.; Widanage, W.D.; Kendrick, E. Development of Experimental Techniques for Parameterization of Multi-Scale Lithium-Ion Battery Models. *J. Electrochem. Soc.* **2020**, *167*, 080534. [CrossRef]
43. Wildfeuer, L.; Wassiliadis, N.; Karger, A.; Bauer, F.; Lienkamp, M. Teardown Analysis and Characterization of a Commercial Lithium-Ion Battery for Advanced Algorithms in Battery Electric Vehicles. *J. Energy Storage* **2022**, *48*, 103909. [CrossRef]
44. Rankin, D.W.H. CRC Handbook of Chemistry and Physics, 89th Edition, Edited by David R. Lide. *Crystallogr. Rev.* **2009**, *15*, 223–224. [CrossRef]
45. Sunderlin, N.; Colclasure, A.; Yang, C.; Major, J.; Fink, K.; Saxon, A.; Keyser, M. Effects of Cryogenic Freezing upon Lithium-Ion Battery Safety and Component Integrity. *J. Energy Storage* **2023**, *63*, 107046. [CrossRef]